Materials and Solidification

Research Article

Experimental and numerical study of thermal and mechanical properties of porous materials based on triply periodic surfaces

Anton V. Eremin[1], Mikhail A. Frolov[2], Alexander F. Krutov[2,3], Mikhail I. Smolkov[2,3,✉], Dmitry M. Bragin[1], Andrey I. Popov[1]

Cite this article: Eremin A, Frolov M, Krutov A, et al. *Materials and Solidification* 2025, **1**(1): 9580001. https://doi.org/10.26599/MAS.2025.9580001

ABSTRACT: 3D models of porous structures were generated based on eight triply periodic surfaces (TPSs) and studied their thermal and mechanical properties. TPSs were derived from topological network representations of zeolite crystal structures via a previously developed method. The resulting TPSs correspond to P, C(P), and IW-P topological types. We developed software for the preparation of TPS models for 3D printing, simulated the corresponding porous materials, and computed their physical properties. We manufactured porous materials for three TPSs via 3D printing with styrene butadiene styrene and polyamide PA-12. The PA-12 samples were formed from the liquid phase, and their solidification occurred under UV radiation. The thermal and mechanical properties of the manufactured samples were studied numerically and experimentally. The results of the modeling were in good agreement with the experimental results.

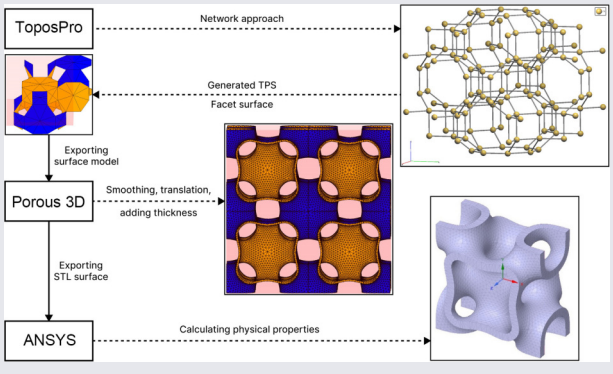

KEYWORDS: triply periodic surfaces (TPSs); porous materials; additive manufacturing (AM); thermal conductivity; compression stiffness

1 Introduction

Macroscopic cellular and porous structures with pores and cells of different types and sizes have received much attention in modern material science and engineering applications [1]. Ordered porous structures obtained on the basis of smooth triply periodic surfaces (TPSs), including triply periodic minimal surfaces (TPMS) with sufficiently complex and different topological and geometrical structures, form a separate class among them [2–4]. This class of porous structures possesses nontrivial thermal-insulating, vibration-isolating, mechanical and other physical properties; thus, they have become the objects of intense theoretical and experimental studies [5–14]. Notice that it is possible to construct new composites and metamaterials on the basis of these structures [11]. The development of additive manufacturing (AM) technology in recent years has led to new impulses to study the structures obtained from TPSs [8,10]. AM allows the production of products with complex topological types and geometrical shapes with layer-by-layer solidification under optimal conditions.

Moreover, the current utilization of TPSs for the development of porous structures is limited to a small number of TPSs suitable for AM, thus emphasizing the importance of generating new TPSs [15]. On the basis of [16,17], we recently proposed a novel approach for creating TPSs and corresponding porous structures on the basis of a topological description of the atom networks of natural crystals, particularly zeolites [18,19]. In fact, our method provides the possibility of obtaining unlimited quantities of different TPSs from periodic network templates via the ToposPro software package [20]. Porous structures derived from TPSs can be produced by AM technology, and their mechanical properties can be studied experimentally or estimated in the most common software packages, such as ANSYS [21], as we did in Ref. [19], with data from [22]. Several recent studies have also focused on creating new TPS/TPMSs [23–27]. In particular, another method that uses the ToposPro package was proposed to simulate the porous space [23]. In this method, TPS is constructed as a surface of equal electron density in the atom lattice of some crystals, which is calculated via the DFT approach and requires considerable computational time. One more method for generating porous structures uses Voronoi diagrams and Delaunay triangulations [24], but it is limited to disordered two-

[1] Heat Power Department, Samara State Technical University, Samara 443100, Russia. [2] Samara Center for Theoretical Materials Science, Samara State Technical University, Samara 443100, Russia. [3] Research Laboratory of Computational Geometry and Theoretical Materials Science, Povolzhskiy State University of Telecommunications and Informatics, Samara 443010, Russia.

✉ Corresponding author. E-mail: m.smolkov97@gmail.com

Received: November 12, 2024; Revised: December 11, 2024; Accepted: December 22, 2024

dimensional structures, whereas our approach produces ordered 3D porous structures. Known TPMSs can also be used to generate porous materials [25,27], but in this case, minimal surfaces must be specified by analytical formulae, and the minimality of the resulting structures is not always guaranteed [25].

In the present work, we produced eight models of porous structures from various zeolite crystals [22]: sodite (SOD), rhodonite (RHO), Linde type A (LTA), Mg-BCCT (BCT), STA-6 (SAS), merlinoite (MER), MAPO-39 (ATN), and CoAPO-CJ62 (JSW). The zeolite-based structures generated varied by topological type, genus, spatial group, labyrinth net topology, Hopf's net topology, and balance properties. The choice of zeolites and the corresponding TPS in this work was conditioned by the problem of establishing correlations between the topological features of the surface and its thermal and mechanical properties. We developed software for the preparation of TPS models for 3D printing, simulated the corresponding porous structures, and computed their physical properties. Furthermore, we created 3D printed samples of different shapes and sizes via an SBS filament and PA-12 polyamide for three zeolite-based structures (SOD, MER, and JSW). In the next stage, we studied the thermal properties of the obtained new structures, particularly the temperature fields, heat flow fields and effective thermal conductivity coefficients. An experimental investigation of the samples obtained via 3D printing methods was also carried out. The experimental measurements of the thermophysical properties were shown to be in good agreement with the theoretical calculations. In addition to the thermophysical properties, the mechanical parameters of cuboid porous samples from PA-12 were measured, and the results were in good agreement with the values calculated via ANSYS software.

The structure of the paper is as follows. In Section 2, the method for generating triply periodic nets via the ToposPro program package and the technique for the construction of porous structures based on these nets in a format available for additive manufacturing are described. Section 3 is devoted to numerical modeling of the thermal properties of the porous structures discussed in this paper as well as experimental verification of the numerical models used. In Section 4, the numerical modeling and experimental measurement of the mechanical properties are discussed. In Section 5, the main results of the work are summarized.

2 Generation of porous materials from TPS derived from atomic nets of crystals

In this work, the procedure for generating porous structures from TPSs is implemented in a software package based on a new network approach for generating triply periodic surfaces from the crystal structures of chemical compounds [18]. This approach, which was implemented in the ToposPro package, includes these consecutive steps:

(i) First, via the universal domain algorithm [28] (left side in Fig. 1), a periodic net is constructed for a given crystal structure.

(ii) Second, a natural tiling for the obtained periodic net is generated [29]. The aforementioned tiling comprises polyhedral cages, referred to as natural tiles, that are surrounded by periodic net rings (natural tile faces) and designated by facial symbols [A^x, B^y, C^z, etc.], where A, B, C, etc. are the sizes of the rings, and x, y, z, etc. are the numbers of rings of a given size in the tile. Symmetry-independent rings of a particular size A are designated Aa, Ab, Ac, etc. (middle in Fig. 1). The inherent characteristic of natural tiles is their role as fundamental (minimal) cages from which any other cage can be constructed by combining multiple natural tiles.

(iii) Finally, create TPSs through the process of enumerating all possible ways of eliminating natural tile faces from the initial tiling while ensuring that the set of remaining faces adheres to three specific conditions:

(a) The decoration condition mandates that all vertices and edges must be positioned on TPS;

(b) the edge condition, which requires that any edge of the net is shared by two faces from the set;

(c) The vertex condition is used to ensure that all edges having a common vertex belong to different pairs of faces. These conditions allow the resulting series of faces to form a single TPS without self-intersections (right side in Fig. 1).

The resulting TPS divides the space into two nonintersecting parts (labyrinth), and if they are isomorphic to each other, the TPS is considered to be balanced [30]. Geometrically, the obtained TPS has a faceted structure and requires smoothing to obtain the minimum mean curvature. Since the number of periodic nets is infinite and more than 800,000 of them are stored in the TopCryst database [26], this approach has been used as a template for generating porous structures and metamaterials. In addition, a database of computer models of some newly discovered TPSs has been created [18]. In this study, we fabricated porous materials from this database (Fig. 2).

Let us discuss this procedure in more detail. The TPS facet model generated by ToposPro is output to a textual.t3g file, where the coordinates of all the facets (rings) are given (Fig. 3):

i) Obtained from the periodic net tiling name (MER) and all of its independent (symmetry inequivalent) rings (4*c*, 8*a*, 8*c*), which were used to compose the tiling (Fig. 3, line 1).

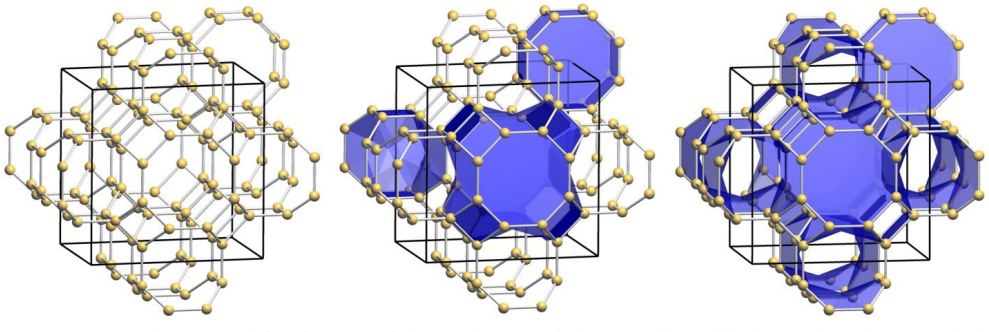

Fig. 1 Zeolite merlinoite (MER) crystal structure: (left) a fragment of the periodic net with the unit cell; (middle) three independent natural tiles with facial symbols [4^2, 8^4] (left tile), [4^{12}, 8^6] (central tile) and [4^8, 8^2] (top right tile); the tiles are confined by three kinds of 4-membered (4*a*, 4*b*, 4*c*) rings and three kinds of 8-membered (8*a*, 8*b*, 8*c*) rings of the net; (right) the triply periodic surface generated by removing two kinds of 4-membered rings (4*a* and 4*b*) and one kind of 8-membered ring (8*b*) and represented by the 4*c*-, 8*a*-, and 8*c*-facets.

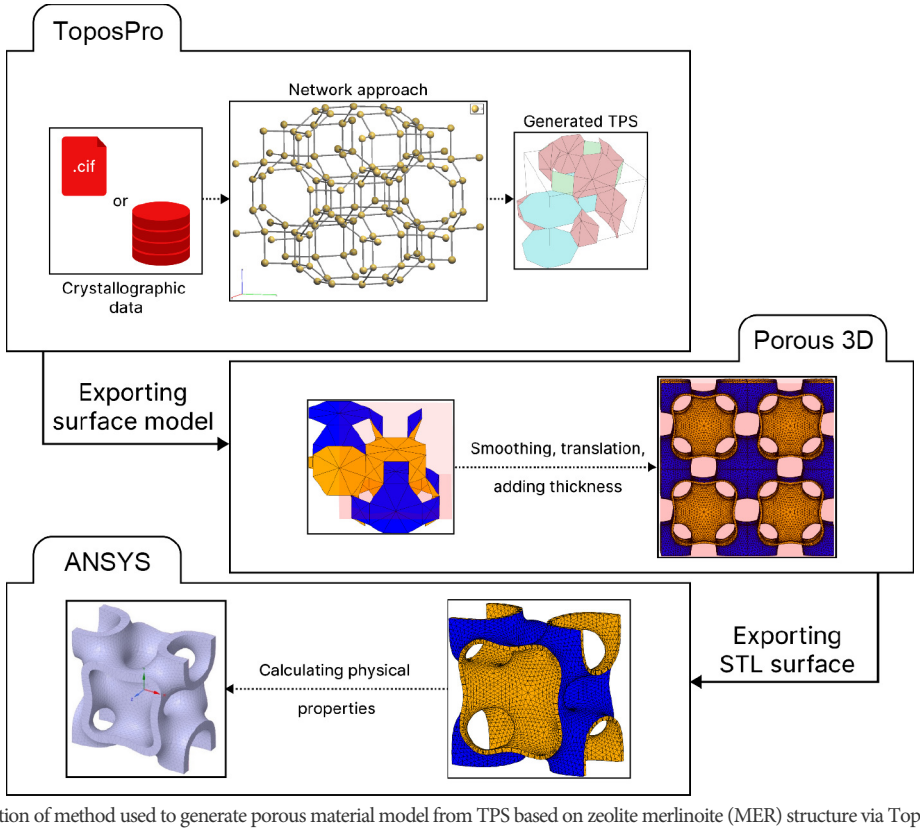

Fig. 2 Visual representation of method used to generate porous material model from TPS based on zeolite merlinoite (MER) structure via ToposPro, Porous 3D, and to numerically study its mechanical and thermal properties with ANSYS software.

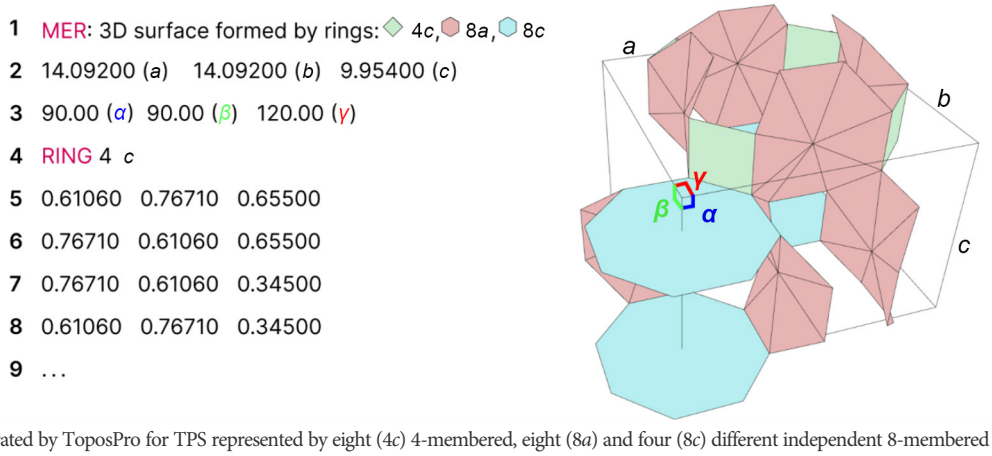

Fig. 3 t3g file generated by ToposPro for TPS represented by eight (4*c*) 4-membered, eight (8*a*) and four (8*c*) different independent 8-membered rings of periodic net obtained for zeolite merlinoite (MER) crystal structure as well as the dimensions and angular parameters of unit cell.

ii) Unit cell parameters (Fig. 3, lines 2–3).

iii) Facet (tile) vertex data (coordinates in fractions of the unit cell dimensions) starting with the keyword RING and its facial symbol (Fig. 3, lines 5–8). These data are present for all the facets in the unit cell.

Previously developed Porous 3D software [31] was used to visualize, translate, smooth and thicken the TPS model imported from the ToposPro.t3g file. The resulting models can be exported to 3D printable STL-format files, which are commonly supported by many computer-aided design and engineering software. Notably, the STL format is used in our algorithms only in exporting the model to various CAD and CAE programs or for 3D printing, and we do not manipulate the geometry of the output STL file. The following algorithms are implemented in this software:

– *Model translation algorithm* (Fig. 4). The unit cell of the imported TPS frame is a translationally independent part of infinite TPS. Obtaining larger parts of an infinite TPS implies parallel translation in space in the rectangular coordinate system (*x*, *y*, *z*) of copies of a unit cell and "gluing" their boundaries. The following method is implemented analytically. Let M be the model that needs to be translated and $v^i \in M$ be a vertex of this model with (v^i_x, v^i_y, v^i_z) coordinates. To translate M, we need to calculate the translation matrix ($\boldsymbol{T}$) on the basis of the unit cell parameters a, b, c, α, β, and γ (Eq. (1)):

$$\boldsymbol{T} = \begin{pmatrix} 1 & 0 & 0 & t_x \\ 0 & 1 & 0 & t_y \\ 0 & 0 & 1 & t_z \\ 0 & 0 & 0 & 1 \end{pmatrix} \quad (1)$$

$$t_x = \begin{bmatrix} a \\ b\cos\gamma \\ c \end{bmatrix}, t_y = \begin{bmatrix} a\cos\beta \\ b \\ c\cos\alpha \end{bmatrix}, t_z = \begin{bmatrix} a\cos\alpha \\ b\cos\beta\cos\gamma \\ c \end{bmatrix}$$

Therefore, using the calculated matrix, we can translate the copied M vertices (M_{copied}) in any direction along t_x, t_y, and t_z as Eq. (2):

$$\boldsymbol{TM}(i) = \begin{pmatrix} 1 & 0 & 0 & n_x t_x \\ 0 & 1 & 0 & n_y t_y \\ 0 & 0 & 1 & n_z t_z \\ 0 & 0 & 0 & 1 \end{pmatrix} \begin{pmatrix} v_x^i \\ v_y^i \\ v_z^i \\ 1 \end{pmatrix} = \begin{pmatrix} v_x^i + n_x t_x \\ v_y^i + n_y t_y \\ v_z^i + n_z t_z \\ 1 \end{pmatrix} \quad (2)$$

$$M_{\text{copied}} = \begin{bmatrix} v_x^i + n_x t_x \\ v_y^i + n_y t_y \\ v_z^i + n_z t_z \end{bmatrix}$$

where n_x, n_y, and n_z are the numbers of models needed along the translation vector (Fig. 4).

– The algorithm for facet smoothing (Fig. 4) uses both Laplacian-based and optimization-based methods to minimize the absolute difference between the maximum and minimum values of the mean curvatures calculated at each vertex of the surface mesh [18]. The mean curvature is calculated via Delaunay triangulation and the theory of normal cycles of differential geometry [32]. We have not used the Laplacian, Taubin, or other smoothing algorithms in their pure form because these algorithms do not account for the mean curvature of the surface. The smoothing algorithm should be applied to the surface mesh, which has no volume; thus, there is no need to preserve the volume of the object, as the mentioned algorithms require. We have checked our algorithm on the surfaces reported in Ref. [18] and found effective accuracy, with an average deviation of the calculated mean curvature of 0.01%.

– Assigning surface thickness is carried out by moving copied points of the surface along their normal vector to the specified distance and restoring surface faces on the moved points. Then, additional polygons are created to fill the gap between the original surface and the copy, resulting in a contiguous volume (Fig. 5). We limit the thickness value of the model to avoid self-intersections in the case of too drastic a change in the surface curvature. We plan to improve the algorithm and remove this limitation in the next version of the Porous 3D software.

The surfaces constructed in this work via the described method are shown in Table 1 and Fig. 6. The thermal and mechanical properties of these surfaces are studied below. In Ref. [19], we investigated the mechanical properties of structures on the basis of only minimal surfaces generated from zeolites via our method. In the present work, the choice of zeolites for constructing surfaces was carried out in terms of establishing correlations between physical properties and surface symmetry properties. Therefore, we chose two zeolites with a high cubic symmetry of atomic networks (space group No. 229), one zeolite with a network close to them (space group No. 221), four zeolites with a lower tetragonal symmetry (space group No. 139) and one zeolite with sufficiently low rhombic symmetry (space group No. 61). The topological structures of the resulting surfaces were established via the ToposPro software package.

As shown in Table 1, surfaces belong to three well-known types: P-surfaces, which are complementary to P-surfaces (C(P) or the Neovius surface), and the I-WP surface [18,33]. All the obtained surfaces have a system of two nonintersecting labyrinths with different balance properties.

Now, let us discuss the relationship of the surfaces from Table 1 with the surfaces from the minimal surfaces database [34], which implements the methods from Ref. [33]. Only the SOD surface from Table 1 is fully equivalent to the corresponding surface from Ref. [34]. The rest of the surfaces, although having the same topology as the corresponding surfaces from Ref. [34], differ from them geometrically and are new. We note once again that the surfaces obtained in this work are closest to the minimum ones, since in our facet smoothing algorithm (Fig. 5), the condition of the minimum modulus of mean curvature is implemented. Using the SpaceClaim module of ANSYS [21], the porous structure is converted to a solid-state geometry (Parasolid) format to numerically investigate its physical properties.

All the calculated topological and geometrical features of the 98 TPSs described in Ref. [18] (Supplementary Information) were used to determine which known TPMSs can be generated with the zeolite dataset. Let us briefly recall the definitions of the topological features used. The labyrinth net topology is the topology of the graph representing two independent pore systems of a generated TPS. Hopf ring net (HRN) topology is the topology of the graph whose vertices coincide with the barycenters of the

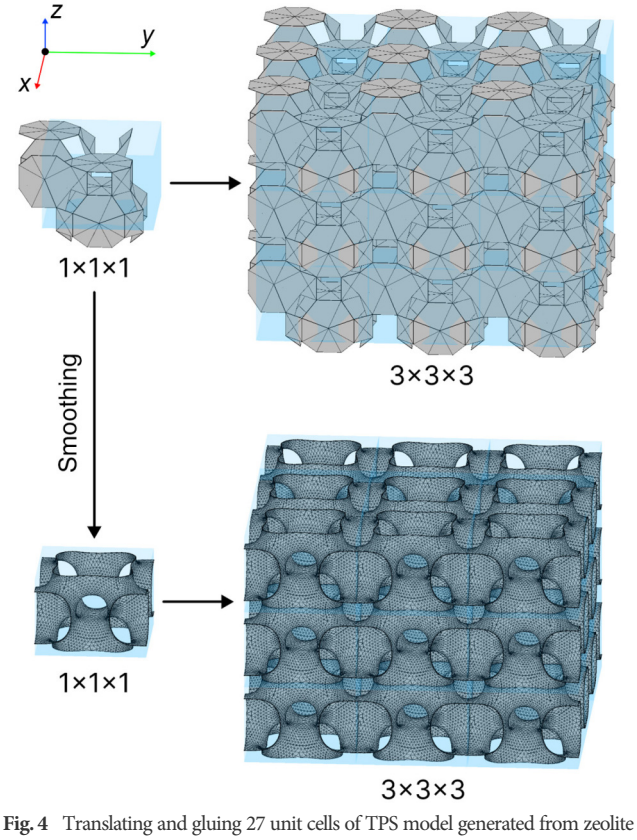

Fig. 4 Translating and gluing 27 unit cells of TPS model generated from zeolite merlinoite (MER) net. Boundaries of internal unit cells (highlighted in light blue on the left) were removed after translation.

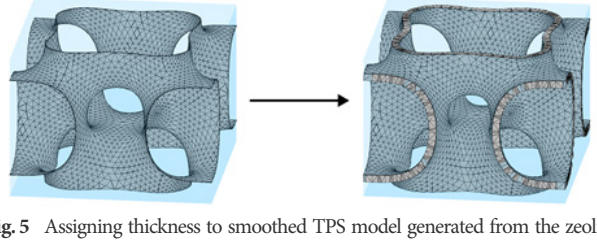

Fig. 5 Assigning thickness to smoothed TPS model generated from the zeolite merlinoite (MER) net.

Table 1 Topological and geometrical features of TPSs used in this work (Fig. 6)

Surface (zeolite)	TPMS analog	Space group	Genus	Labyrinth nets topology	Hopf ring net (HRN) topology	Balanced property	Tiling rings type
SOD	P	$Im\bar{3}m$	3	pcu; pcu	(nbo)	True	6*a*
RHO	C(P)	$Im\bar{3}m$	9	ftw;ftw	(14^2, 16, 22, 28^3, 32^2, 36, 44, 46, 50, 52, 56, 58, 60^3, 62, 66, 68-*c*)	True	4*b*, 6*a*, 8*a*
LTA	P	$Pm\bar{3}m$	3	pcu; pcu	(nbo)	True	4*b*, 6*b*
BCT	P	*I*4/*mmm*	3	pcu; pcu	(nbo)	True	8*c*
SAS	P	*I*4/*mmm*	3	pcu; pcu	(nbo)	True	4*a*, 4*b*, 6*a*
MER	I-WP	*I*4/*mmm*	4	nbo;bcu	(4, 6^3, 8^2, 12, 14-*c*)	False	4*c*, 8*a*, 8*c*
ATN	P	*I*4/*mmm*	3	pcu; pcu	(nbo)	True	4*a*, 8*b*
JSW	P	*Pbca*	3	pcu; pcu	(nbo)	True	4*a*, 4*b*, 4*c*, 6*c*, 6*d*

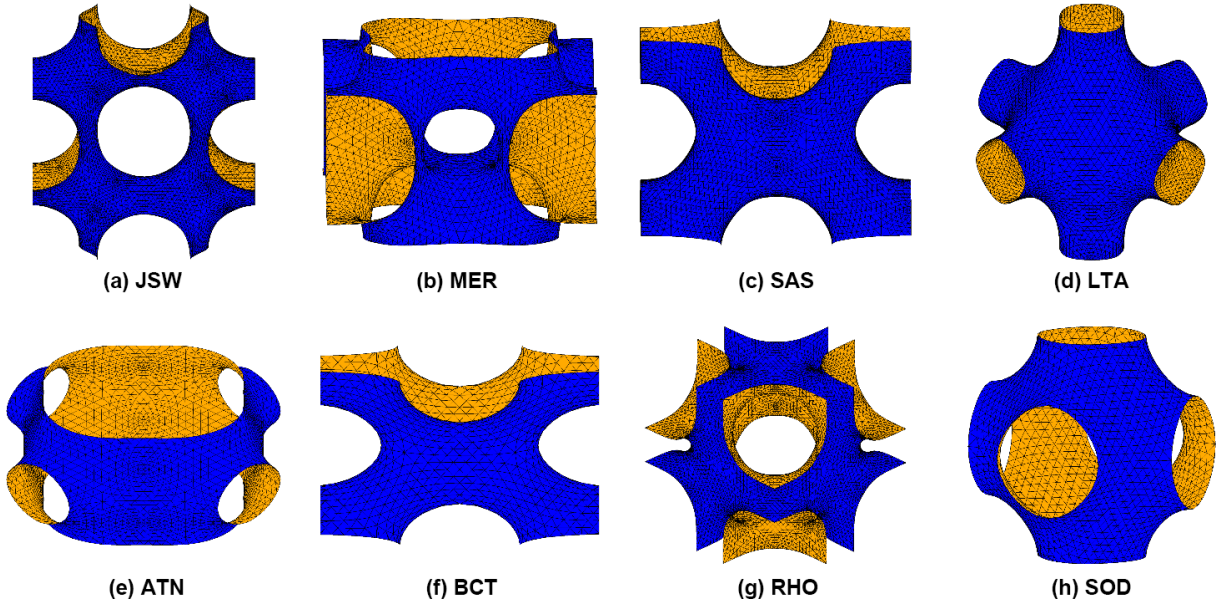

Fig. 6 Unit cells of TPSs present in this work. (a) TPS (P surface) based on CoAPO-CJ62 (JSW) zeolite; (b) TPS (I-WP surface) based on merlinoite (MER) zeolite; (c) TPS (P surface) based on STA-6 (SAS) zeolite; (d) TPS (P surface) based on Linde type A (LTA); (e) TPS (P surface) based on MAPO-39 (ATN) zeolite; (f) TPS (P surface) based on Mg-BCCT (BCT) zeolite; (g) TPS (C(P) Neovius) based on Rho (RHO) zeolite; (h) TPS (P surface) based on sodalite (SOD) zeolite.

TPS rings and the barycenters of catenated rings, which are built on the geometrical centers of the rings of the labyrinth net. The HRN is used to determine the method of interweaving the labyrinth nets. The TPS is balanced if it divides the space into two congruent labyrinths. All the features described above are crucial for determining known TPMS analogs of our surfaces, i.e., P, C(P), I-WP, F-RD, G, H, and other TPMSs.

Below, we consider how this method can be applied to investigate the thermophysical and mechanical properties of TPSs, as shown in Table 1. Note that other recent studies [5,6,8–12,35–37] where the porous structures were modeled from TPS applied analytical formulae for constructing these known TPSs. All of the surfaces generated by our method (see Table 1) cannot be created by existing methods, especially new minimal surfaces. The described method constructs TPSs based on crystal structure, so surfaces are unique in their geometry even if their topological properties are similar to those of existing surfaces and are not described by any analytical expressions.

The presented method does not require any analytical representations to generate TPSs, and the new TPSs obtained via our approach also do not yet have any exact formulae. Therefore, the theoretical part of our study included the following stages:

i) The TPS frame is generated from the periodic net obtained from crystal structure data using ToposPro and then exported into a ".t3g" file.

ii) Imported in Porous, the 3D TPS is then processed by the developed algorithms and saved as an .stl model file.

iii) Using ANSYS, we numerically investigate the thermophysical and mechanical properties of the obtained ".stl" model as described below.

3 Experimental and numerical studies of thermophysical properties of obtained porous structures

In this work, we investigate the effective conductivities of porous structures with novel triply periodic solid shell architectures. Despite the ordered macrostructure, the thermal properties of porous materials cannot be considered isotropic. The thermal conductivity values that characterize heat transfer are different at different points in the medium and depend on the heat transfer direction.

The thermophysical properties of isotropic bodies can be identified by solving the inverse thermal conductivity problem. However, the problem becomes much more complicated for anisotropic materials, which is the case in our study since the periodic TPS structure tends to have a high degree of anisotropy in the sample.

Fourier's law is formulated in an anisotropic media as Eq. (3):

$$\boldsymbol{q} = -\boldsymbol{k}\nabla u \tag{3}$$

where $\boldsymbol{q}$ is the heat flux vector, $\boldsymbol{k} = [k_{ij}]\ (i,j = \overline{1,3})$ is the symmetric thermal conductivity second-rank tensor, and ∇u is the temperature gradient.

With Eq. (3), the energy conservation equation (heat equation) can be written as Eq. (4):

$$\rho c_p \frac{\partial u}{\partial t} = -\mathrm{div}\,(-\boldsymbol{k}\nabla u) + q_V \tag{4}$$

where c_p is the specific heat capacity, ρ is the material density, t is the time, u is the temperature, and q_V is the internal heat energy per unit volume at each point and time.

Since the thermal conductivity $(-\boldsymbol{k})$ is a tensor, the heat fluxes at each point in the area under study are different in different directions. It follows from Eq. (4) that to account for the property anisotropy, one needs to solve multidimensional equations containing mixed differential operators. Additional difficulties arise when setting the boundary conditions for Eq. (4) since the heat fluxes need to be determined while taking into account the boundary behavior, i.e., the direction cosines to the boundary with respect to the selected coordinate system [38].

The difficulties mentioned above significantly limit the possibility of applying classical analytical methods for the theoretical evaluation of the thermal conductivity tensor elements $[k_{ij}]\ (i,j = \overline{1,3})$. In this context, various methods of medium homogenization are used to describe the temperature state of anisotropic media: RVE, MsFEM, etc.

Thus, the representative volume element (RVE) method is introduced, where RVE is the minimum volume of an anisotropic body that reproduces its thermal properties [39]. M. I. Epov *et al.* [40] used the multiscale finite element method (MsFEM), etc. In this work, we use the RVE method of medium homogenization. Note that in our approach, the computer representation of new porous structures enables one to easily implement any method of medium homogenization, including the RVE method, although for most of our surfaces, there is no representation in the form of an analytical expression.

To determine the integral thermal characteristics of a unit cell element, for example, of the MER-based TPS (Fig. 7) along the z-axis, we assume that the thermophysical properties at any point in the unit cell volume are isotropic. That is, we consider the volume under study to be filled with a homogeneous medium with constant effective thermal conductivity and an effective coefficient of thermal conductivity (k_{eff}). The anisotropy of properties caused by the features of 3D printing via the FDM method has a great influence on the results of experimental studies. In particular, when the thermal conductivity of samples in which the rasters are oriented along and perpendicular to the direction of heat flow is studied, differences in measurements can reach 50%. Notably, the smallest deviation from the thermal conductivity of the original material is observed when rasters lie in the direction of heat flow. Studies [41,42] have shown that with an optimal raster direction and a 100% fill ratio, the discrepancy between the thermal conductivities of the original material and the sample does not exceed 5%–10%. In this work, for an experimental study of thermal conductivity, samples whose raster direction coincided with the direction of heat flow at a 100% fill ratio were used. In this way, the error caused by anisotropy is minimized and is acceptable for research purposes.

If heat transfer occurs only along the z-axis, the heat flow (Q) across any orthogonal section of the unit cell is determined via Eq. (5):

$$Q = \overline{q_s} S \tag{5}$$

where

$$\overline{q_s} = \frac{1}{S}\int_{\sigma} q\,\mathrm{d}\sigma \tag{6}$$

where $\bar{q}_s$ is the average density of heat flux in the cross-section ($S = ab$), q is the actual density of heat flux in the cross-section ($\sigma = S(1-s)$), $s(= S_{\mathrm{l}}/S)$ is the specific pore area, and S_{l} is the pore area in the cross-section under consideration.

However, according to Fourier's law (Eq. (7)):

$$\overline{q_s} = -k_{\mathrm{eff}}\frac{\partial u}{\partial z} \tag{7}$$

It follows from Eq. (4) that for the stationary mode of heat transfer, the temperature distribution in the homogenized medium along the z coordinate changes according to a linear law. Then, Eq. (8) is valid.

$$\overline{q_s} = -k_{\mathrm{eff}}\frac{u_2 - u_1}{a} \tag{8}$$

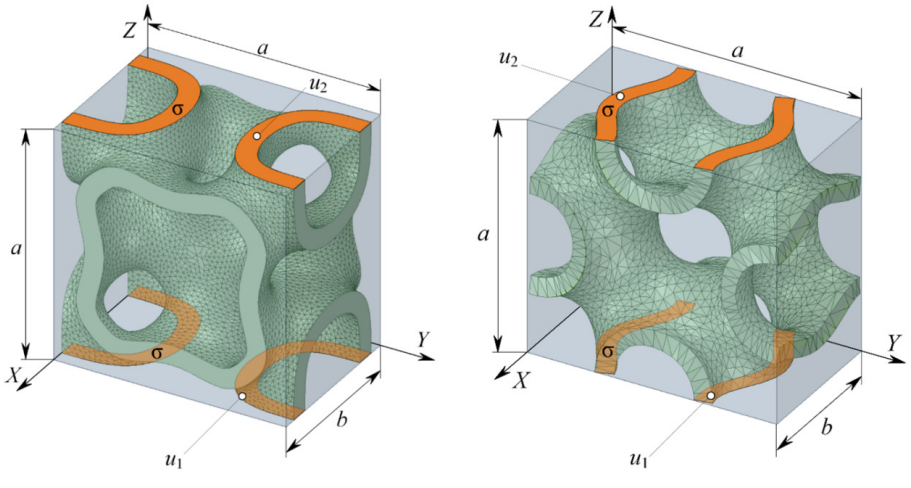

(a) MER–based structure (b) JSW–based structure

Fig. 7 RVE scheme with the inscribed solid shell. (a) Merlinoite (MER-based) structure and (b) CoAPO-CJ62 (JSW-based) structure where u_1 and u_2 are the boundary temperatures and where σ is the area of the unit cell in the cross section.

where u_1 and u_2 are the temperatures at the cell boundaries.

Given that $S = ab$, we have the following from Eqs. (6) and (8):

$$k_{\text{eff}} = \frac{\overline{q_s}a}{u_2 - u_1} = \frac{\int_\sigma q \mathrm{d}\sigma}{b(u_2 - u_1)} \tag{9}$$

To determine the actual value of the heat flux in the cross-section perpendicular to the z-axis, we use the specific surface of the pores (s). Analysis of the dependence $s(Z, \Delta)$ (Fig. 8) reveals that the pore is symmetrical with respect to $Z = 0.5$, with equal s values at $Z \in [0; 0.5; 1]$. This can be explained by the fact that the creation of pores in the principal direction leads to the formation of two independent pore systems. The average density of the heat flux ($\overline{q_\sigma}$) is as Eq. (10):

$$\overline{q_\sigma} = \frac{\overline{q_S}}{1 - s} \tag{10}$$

which can be determined from ANSYS numerical modeling as the average heat flux, is greater than the corresponding $\overline{q_S}$ value at any point of the S cross-section.

Given Eq. (10), the equivalent thermal conductivity is determined via Eq. (11):

$$k_{\text{eff}} = \frac{a\overline{q_\sigma}(1 - s)}{u_2 - u_1} \tag{11}$$

The unit cell shown in Fig. 7 is an RVE-element. Therefore, the determination of its thermal characteristics allows one to describe the temperature state of media consisting of many unit cells subject to perfect thermal contact. Obviously, we can obtain structures with specified thermal characteristics by combining the unit cells as well as changing the wall thickness of the solid shell and the cell size.

We applied the following conditions for the CAE modeling of heat transfer in ANSYS:

(i) the heat transfer mode is stationary;

(ii) heat transfer occurs along one of the axes of the orthogonal coordinate system (specifically, the z-axis);

(iii) the first-type boundary conditions, temperatures $u_1 = 0$ °C and $u_2 = 100$ °C, are set on the upper and lower faces of the solid shell, respectively (Fig. 7);

(iv) An adiabatic wall condition is set on the entire surface of the solid shell except for the top and bottom faces;

(v) The thermophysical properties of the solid shell are known (Table 2).

On the basis of condition (ii), the heat transfer along the x- and y-axes can be ignored. According to condition (iv), we neglect convective heat transfer. This assumption does not significantly affect the accuracy of modeling for natural convection in the pore space (at $a < 5$ mm).

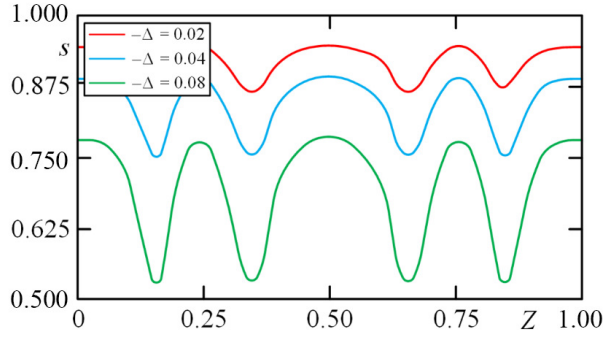

Fig. 8 Dependence of s on $Z = z/a$ for different values of specific wall thickness $\Delta = \sigma/a$ along the z-axis.

The calculation results for the scalar temperature field (Fig. 9) and the vector field of heat flux (Table 3) enabled us to study the behavior of k_{eff} when the unit cell size (a) and wall thickness (σ) of the material were changed.

The dependence $k_{\text{eff}}(\Delta)$ is linear (Fig. 10), while scaling the unit cell results in a proportional change of k_{eff}; for example, $k_{\text{eff}}(\Delta) = 2k_{\text{eff}}(2\Delta)$. The relationship between the volume and surface area as the size of TPMS increases or decreases has been described by the square–cube law.

The analysis of Fig. 10 shows that a required value (k_{eff}) can be obtained by changing the wall thickness (σ) or the unit cell size (a). For example, a value of $k_{\text{eff}} = 0.0159$ for MER-based material along the z-axis can be obtained at a relative pore wall thickness $\Delta = 0.03$, which can be defined as $\sigma/a = 0.15/5 = 0.3/10$, etc. Therefore, a material with calculated thermophysical properties can be created by changing the structural macroparameters of the unit cell.

When choosing the configuration of a porous structure, it is necessary to specify strength indicators. Thus, shrinking the unit cells leads to hardening of the structure. On the other hand, enlarging the unit cell results in increasing the influence of the convective component.

To verify the adequacy of the modeling results, an experimental verification was performed. Using additive printing technology, a panel of a porous material with a size of 200 mm × 200 mm × 20 mm was made by the TOTAL Z Anyform L250G3-2X printer via the FDM method (Fig. 11). When printing, SBS filaments with the properties specified in Table 2 were used. Printing was performed with the following settings: layer height of 0.15 mm; print speed of 15 mm·s^{-1}; nozzle temperature of 220 °C.

The determination of the thermal conductivity coefficients k_{eff} was carried out on a certified experimental setup ITP-MG4, which included a refrigerator and a heater to maintain constant temperatures u_1 and u_2 on the surfaces of the test samples. The thermal conductivity coefficient (k_{eff}) was determined according to Eq. (1), with an error of no more than 5%. By approximating the theoretical and experimental data, we obtain a relation for determining the value of the effective thermal conductivity coefficient at different Δ values (Eq. (12)):

$$k_{\text{eff}}(\Delta) = C_1\Delta + C_2 \tag{12}$$

where C_1 and C_2 are the fitting constants for the function, which are presented in Table 4.

To determine the heat capacity and density, we used the porosity ratio, where $\phi = V_P/V$ is equal to the ratio of the pore volume $V_P = V - V_{\text{structure}}$ to the volume of the entire unit cell. $V_{\text{structure}}$ is calculated via ANSYS methods. For the TPS-based materials, the porosity ($\phi = V_P/V$ where V_P is the pore volume) is a linear function of the relative wall thickness (Eq. (13)):

$$\phi = A_1\Delta + A_2 \tag{13}$$

where A_1 and A_2 are the fitting constants for the function.

Given Eq. (13), the volume heat capacity and density are determined by Eqs. (14) and (15):

Table 2 Thermophysical properties of SBS filaments

Material characteristic	Value	Unit
Type of material	SBS	—
Conductivity coefficient	0.2	W·m^{-1}·°C^{-1}
Heat capacity	1000	J·kg^{-1}·°C^{-1}
Density	1010	kg·m^{-3}

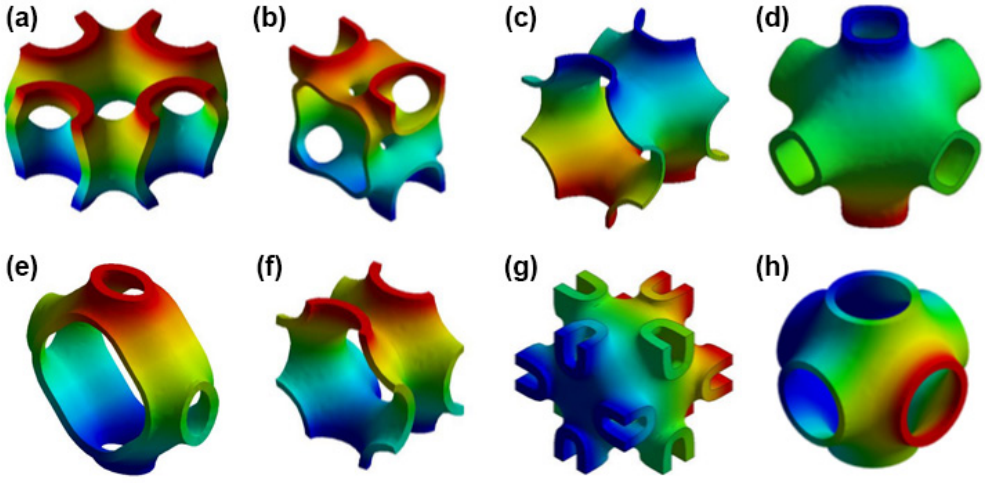

Fig. 9 (a–h) Scalar temperature fields from 0 °C (navy blue) to 100 °C (red) for JSW-, MER-, SAS-, LTA-, ATN-, BCT-, RHO-, and SOD-based structures, respectively.

Table 3 Average heat flux in Eq. (10) for scalar temperature fields (Unit: $W \cdot m^{-1} \cdot °C^{-1}$)

Structure	Along *z*-axis	Along *x*-axis
JSW	3764	6842
MER	3497	4873
SAS	2843	4025
LTA	3893	3893
ATN	3421	9217
BCT	3873	6177
RHO	3836	3836
SOD	3674	3674

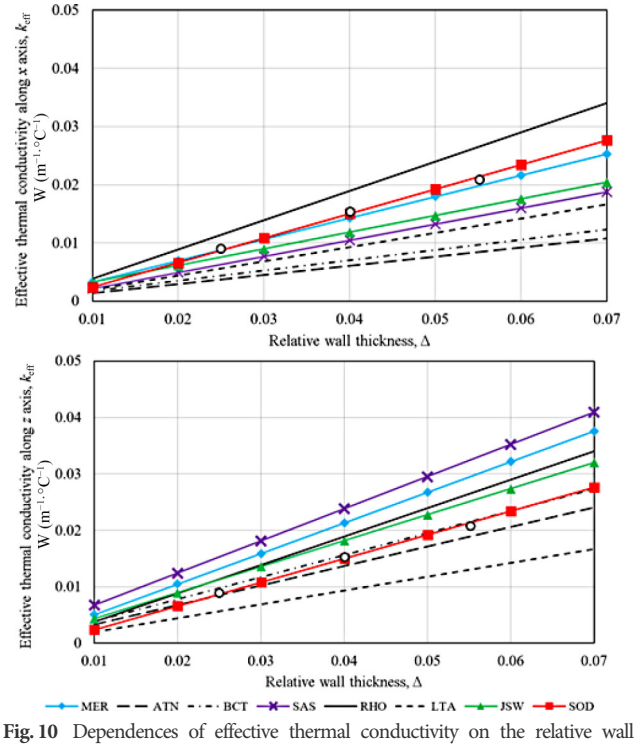

Fig. 10 Dependences of effective thermal conductivity on the relative wall thickness for surfaces from Table 1; white circles represent experimentally obtained data on the effective thermal conductivity of SOD-based structures.

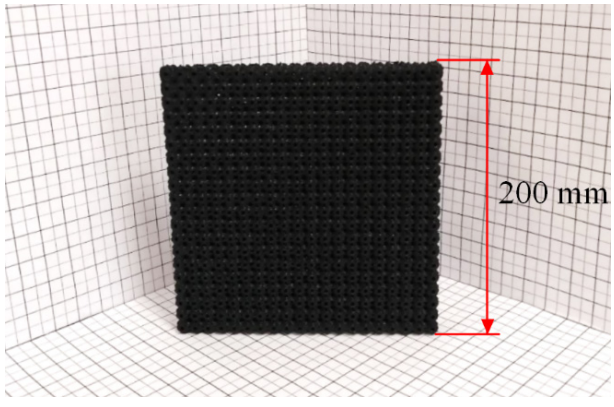

Fig. 11 Sample made of SOD-based porous structure manufactured from SBS by FDM method.

Table 4 Fitting constants of thermal conductivity coefficients ($\boldsymbol{k}_{\mathbf{eff}}$) in Eq. (12) for two different directions

Structure	Along *z*-axis		Along *x*-axis	
	C_1	C_2	C_1	C_2
JSW	0.286	3.593E-04	0.460	−2.695E-04
MER	0.366	−3.593E-04	0.542	−3.593E-04
SAS	0.277	−5.988E-04	0.569	1.018E-03
LTA	0.245	−4.790E-04	0.245	−4.790E-04
ATN	0.157	−2.096E-04	0.345	−1.198E-04
BCT	0.176	−2.994E-05	0.390	2.096E-05
RHO	0.503	−1.198E-03	0.503	−1.198E-03
SOD	0.420	−1.800E-03	0.420	−1.800E-03

Note: the fitting constants are measured in $W \cdot m^{-1} \cdot °C^{-1}$.

$$c = c_m(1-\phi) \tag{14}$$

$$\rho = \rho_m(1-\phi) \tag{15}$$

where c_m and ρ_m are the heat capacity and density of the material, respectively.

Thus, this paper presents the results of comprehensive studies of porous structures based on TPS. The results obtained for SBS can be extended to other structures and other forms of the unit cell. Equations (12)–(15) enable one to determine the properties of

the designed structure with high accuracy without performing additional calculations.

4 Experimental and numerical study of main mechanical properties of obtained porous structures

To investigate the mechanical properties of the atomic RVE structures described in Section 2, porous samples were manufactured via additive technology from the photopolymer resin "Phrozen aqua-gray-resin" (polyamide PA-12) (Fig. 11), the properties of which are given in Table 5. The samples are single RVEs for MER-based and JSW-based structures (see Fig. 12) sewed in three orthogonal directions in amounts of 2 × 2 × 2, 3 × 3 × 3, and 4 × 4 × 4. Single RVEs have length (L) × width (W) × height (H) values of 10.63 mm × 8.83 mm × 10.63 mm and 8.14 mm × 8.14 mm × 4.91 mm for MER-based and JSW-based structures, respectively. The wall thickness of each sample is 0.2 mm.

Using a Phrozen Sonic Mighty 4K LCD photopolymer printer, we produced several samples via layer-by-layer solidification under UV light according to the following recommended settings: maximum layer height of 0.05 mm; number of acceptable substrate words of 6; substrate illumination time of 50 s; remaining layer illumination time of 5 s; maximum lifting height of 8 mm; and lifting and retraction speeds of −60 and 150 mm·min^{-1}, respectively.

The mechanical properties of the samples manufactured from PA-12 significantly depend on the 3D printing mode. Before studying porous samples, experimental measurement of the mechanical characteristics of PA-12 after the 3D printing procedure is necessary. For this purpose, several solid rectangular parallelepipeds, the sizes of which are indicated above, were manufactured via the same technology and equipment.

Following other recent studies of porous structures [7–14], we carried out compression tests on our samples to experimentally measure their mechanical moduli. A tensile testing machine (SHIMADZU) was used to measure the compression characteristics of all the samples in automatic mode. The rate of compression was 1 mm/min. All the measurement errors were less than 0.01%.

Table 5 Properties of PA-12 material

Property	Value	Unit
Density	1.27	g·cm^{-3}
Viscosity	1.5	10^{-1} Pa·s
Tensile elongation	7	%
Tensile strength	0.02	GPa
Hardness	623	HV
Tensile modulus	0.192	GPa
Notched Izod impact strength	6780	J·m^{-2}

The stress–strain curves obtained experimentally were averaged for all similar solid samples. A linear increase in strain was revealed at low deformation stress and plastic strain areas on the graph up to a stress of 49.33 MPa. For such materials, this behavior is typical [43].

Using experimental data, the average value of the elastic compression modulus was E_c = 1.07±0.04 GPa in the range of ε = 1%–3%, and the Poisson's ratio was approximately 0.4. This value falls within the acceptable range of this characteristic for a polyamide polymer at standard room temperature [43].

JSW-based and MER-based samples (Figs. 12(a) and 12(b), respectively) were investigated via a similar experimental technique to that used for continuous samples. The experimental loading curves are shown in Fig. 13. The position of the curves depends on the number of RVEs in the sample, and curves with different numbers of RVEs are similar. The difference in the shape of the curves for the MER-based and JSW-based samples is due to the difference in the topological and geometric features of the corresponding surfaces, as shown in Table 1. Figure 13 shows that the MER-based sample is characterized by the presence of an elastic deformation region and slow growth to a maximum before failure. The JSW-based curve contains a pronounced maximum after the elastic section and subsequent oscillations before destruction. Both of these types of curve behavior take place for

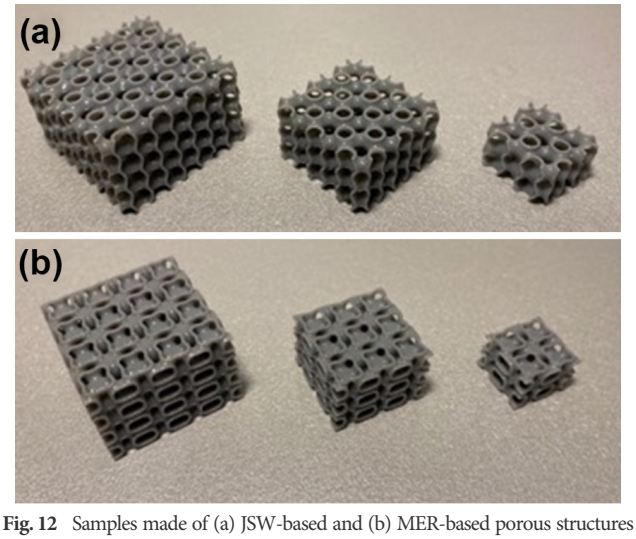

Fig. 12 Samples made of (a) JSW-based and (b) MER-based porous structures manufactured from PA-12.

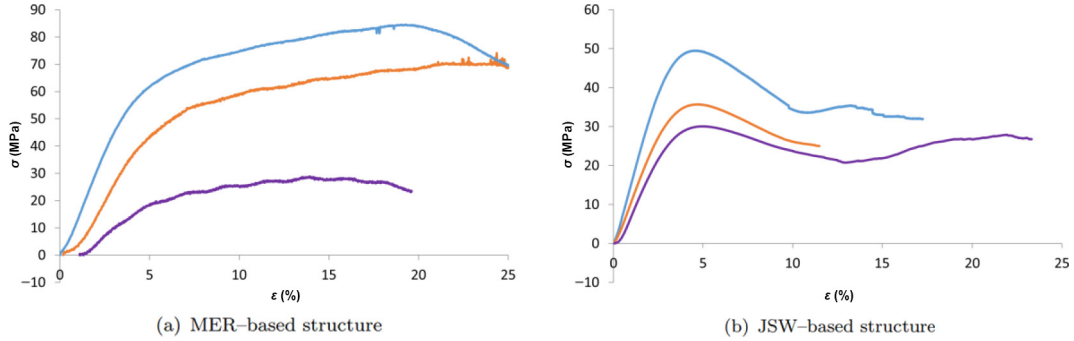

(a) MER–based structure (b) JSW–based structure

Fig. 13 Compressive stress–strain curves for (a) MER-based and (b) JSW-based samples with different numbers of RVEs (see Fig. 12); the upper curves (blue) are 4 × 4 × 4 samples, the middle curves (orange) are 3 × 3 × 3 samples, and the lower curves (violet) are 2 × 2 × 2 samples.

known porous materials obtained on the basis of triply periodic surfaces different from ours [1,11].

The experimental compression moduli (E_c) were obtained by the slope average of the curves within the strain of 1%–2% (Fig. 13). These experimental values are shown in Table 6 together with the results of the corresponding finite element (FE) calculations.

We note fairly good agreement between the experimental and theoretical results for the compression moduli, which indicates the adequacy of the chosen theoretical model.

The FE software ANSYS was used for numerical modeling of the compression test results to determine the elastic properties of the porous MER-based and JSW-based samples, as well as for predicting the mechanical properties of other porous materials (Table 1) when their stress-strain state and geometrical parameters were changed. Our simulation contains two main features. First, we considered polyamide as a material belonging to the class of hard rubber, and only elastic deformations of this initial material were taken into account when modeling the mechanical properties of porous samples. Second, the patch control method was chosen as a method for generating a finite element grid using tetrahedral elements with an average size close to 0.7 mm. However, shell finite elements with a slightly smaller size were used to simulate RVE for the 4 × 4 × 4 samples. The fairly good agreement between the results of the theoretical calculations in the described model and the experimental results (Table 6) makes it possible to model the mechanical properties of other porous materials on the basis of TPS from Table 1 in the same way.

Therefore, the distributions of the von Mises mechanical stresses calculated via the FE method are shown in Fig. 14 for different single RVEs. Fig. 14 shows that the stresses are distributed rather uniformly, which is apparently explained by the proximity of the surfaces constructed in this work to the minimum surfaces, as discussed in Section 2 (see also Ref. [34]). Recall that our smoothing procedure from Section 2 includes the minimum mean surface curvature condition.

The components of the compression and shear modules, as well as the Poisson's ratios for a single RVE (Fig. 14), are presented in Table 7. For all single RVEs, the elastic compression modules (E_{11}, E_{22}, and E_{33}) were calculated along the main axes (Fig. 14). The Poisson coefficients (ν) and shear modulus (G) for the unit RVEs were calculated via Eq. (16):

$$G_{ij} = \frac{\tau_{ij}}{\theta_{ij}}, \quad \nu_{ij} = \frac{\varepsilon_{\text{trans}(i)}}{\varepsilon_{\text{axial}(j)}} \tag{16}$$

where τ is the tangential stress, θ is the tangential relative deformation, and $\varepsilon_{\text{trans}}$ and $\varepsilon_{\text{axial}}$ are the transverse and longitudinal relative deformations, respectively.

However, it should be noted that all these calculations were performed for the fixed thickness of the sample walls and the same initial material and do not have universal meaning. Nevertheless, the data in Table 7 can be used to evaluate the mechanical properties of porous materials relative to each other. For example, the isotropic RHO-based structure is the most stiff in compression, the MER-based structure also exhibits greater stiffness in compression along one of the directions, the ATN-based structure is the most compliant in compression, and the BCT-based structure has the highest shear resistance. Only LTA-based and RHO-based TPMS have identical mechanical parameters along the principal axes, whereas the remaining structures have substantially anisotropic behavior.

To obtain more universal estimates of the mechanical properties of the porous structures listed in Table 1, we used the well-known Gibson–Ashby relation (Eq. (17)) [1]:

$$\frac{E^*}{E_{\text{mat}}} = \left(\frac{\rho^*}{\rho_{\text{mat}}}\right)^{\alpha} \tag{17}$$

where E^* is the compression modulus, ρ^* is the average density of the porous structure; on the other hand, E_{mat} is the compression modulus, ρ_{mat} is the density of the initial material; α is a topological–geometrical parameter, depending mainly on the properties of TPMS.

The functional relation in Eq. (17) does not depend on the type of initial material but is determined by the geometrical and topological characteristics of the porous structure. The main purpose of Gibson–Ash analysis in our work was to compare the mechanical properties of porous samples with different topological and geometrical structures. In this regard, we perform the appropriate calculations only for single RVEs with the topological and geometrical parameters listed in Table 1. Modeling is carried out at small relative deformations during compression in the range of 1%–3%.

The mechanical properties of the skeleton material were described only by its linear (elastic) moduli. Interesting problems of considering nonlinear effects, fatigue effects, and experimental verification of the results are beyond the scope of our paper. The results of the analysis of our calculations via the Gibson–Ash relation in Eq. (17) in the case of compression along the x- and y-axes are shown in Fig. 15. The mutual arrangement of the lines in Fig. 15 corresponds to the trend of the values in Table 7 and is similar to the results from article [11], in principle. Note that the close lines in Fig. 15 can describe the properties of porous structures, the characteristics of which, from Table 1, can be very different. This means that a more detailed description of the topological and geometric properties of the surfaces is needed to establish correlations between the topological–geometric properties of triply periodic surfaces and the mechanical properties of the corresponding porous materials. This will be done by us in the future. Nevertheless, the results shown in Fig. 15 can be used in engineering practice when structural materials with optimal physical and mechanical properties are chosen, for example.

An important feature of porous structures is their ability to absorb strain energy [7–14]. We calculated the dependence of the strain energy density on the relative density for the porous structures constructed in our work (see Table 1). The calculations were carried out for the case of compression along the x- and y-axes. The results of the calculation are shown in Fig. 16. A

Table 6 Experimental and numerical elastic compression moduli (E_c) for MER and JSW samples (Fig. 12) (Unit: MPa)

Sample	E_c (MER)		E_c (JSW)	
	Experiment	FE calculation	Experiment	FE calculation
2 × 2 × 2	6.10±0.21	6.03	7.63±0.25	7.53
3 × 3 × 3	11.95±0.42	12.03	8.43±0.28	8.32
4 × 4 × 4	14.79±0.49	14.86	11.76±0.39	11.64

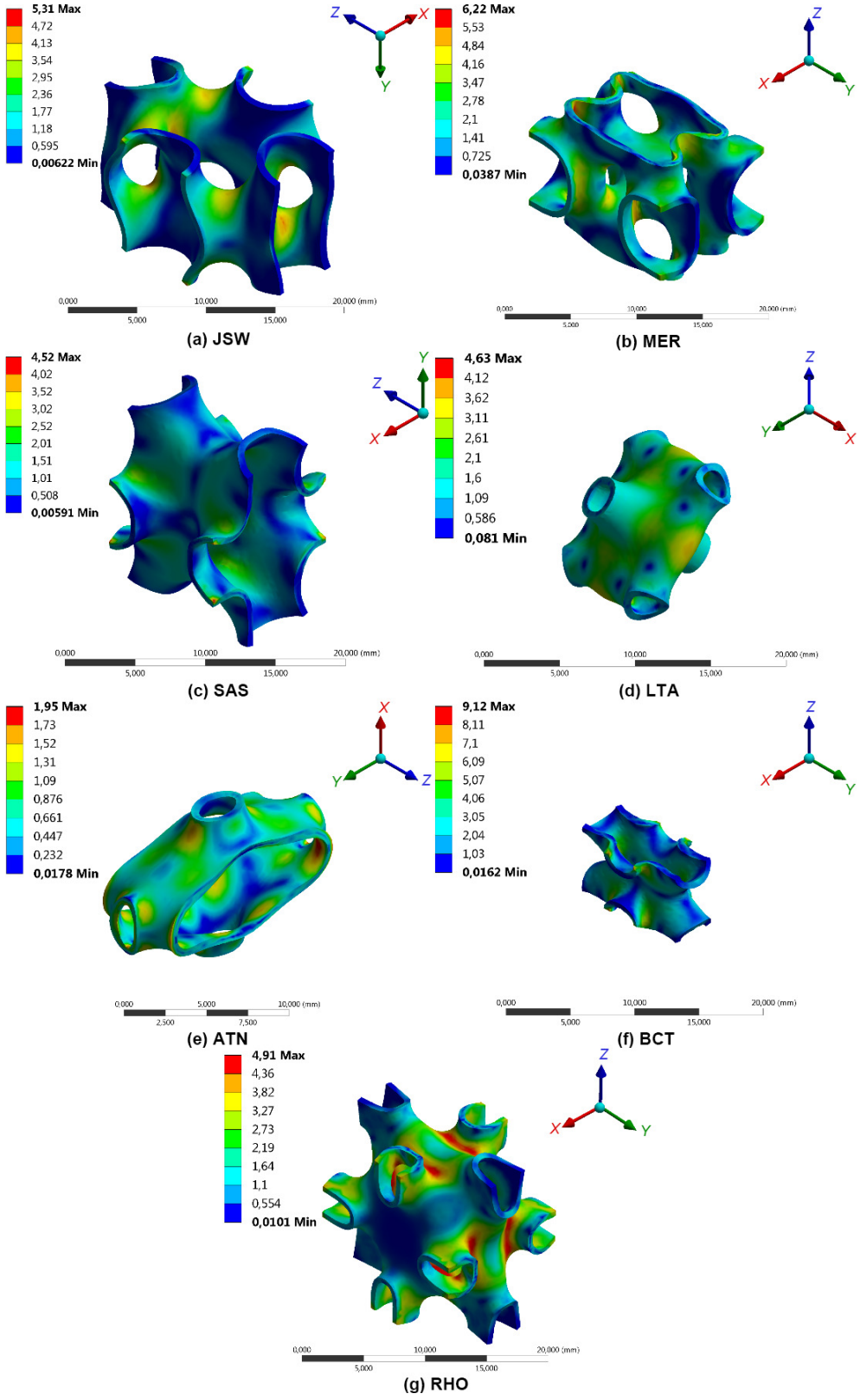

Fig. 14 Distribution of von Mises stresses in modeling compression in ANSYS software via finite element method for different single RVEs with a relative compressive deformation of 3%. (a–g) JSW-, MER-, SAS-, LTA-, ATN-, BCT-, and RHO-based structures, respectively. The red areas have the highest stress, and the blue areas have the lowest stress.

comparison of Figs. 15 and 16 reveals that the sequence of lines is the same. That is, the strain energy density absorbed by the porous structure corresponds to its stiffness. However, the relative distance between the lines in Figs. 15 and 16 can vary significantly. Thus, porous structures with almost the same stiffness can absorb different amounts of strain energy. For example, this is clearly observed when the upper groups of lines in Figs. 15(b) and 16(b) are compared.

Table 7 Mechanical characteristics of single RVE (Fig. 14) obtained via the FE method (Unit: MPa)

Structure	E_{11}	E_{22}	E_{33}	G_{12}	G_{23}	G_{31}	υ_{12}	υ_{13}	υ_{23}
JSW	13.58	11.25	6.98	0.71	5.60	6.24	−0.10	0.79	0.73
MER	12.29	20.30	12.37	4.73	4.73	6.82	0.21	0.59	0.34
SAS	1.37	5.68	1.38	4.49	4.51	6.55	0.10	0.87	0.41
LTA	4.18	4.18	4.18	2.66	2.66	2.66	0.42	0.42	0.42
ATN	0.66	3.80	0.66	4.84	4.86	6.95	0.04	0.96	0.20
BCT	9.18	3.78	9.18	7.91	7.84	14.01	0.52	0.61	0.22
RHO	17.93	17.93	17.93	2.68	2.68	2.68	0.33	0.33	0.33

Note: E_{11}, E_{22}, and E_{33} are the compression modules along the principal axes. The orientation in 3D space of the unit RVEs is shown in Fig. 14. Poisson's ratios (υ) and shear moduli (G) are defined by Eq. (16). The thickness of the wall is 0.2 mm.

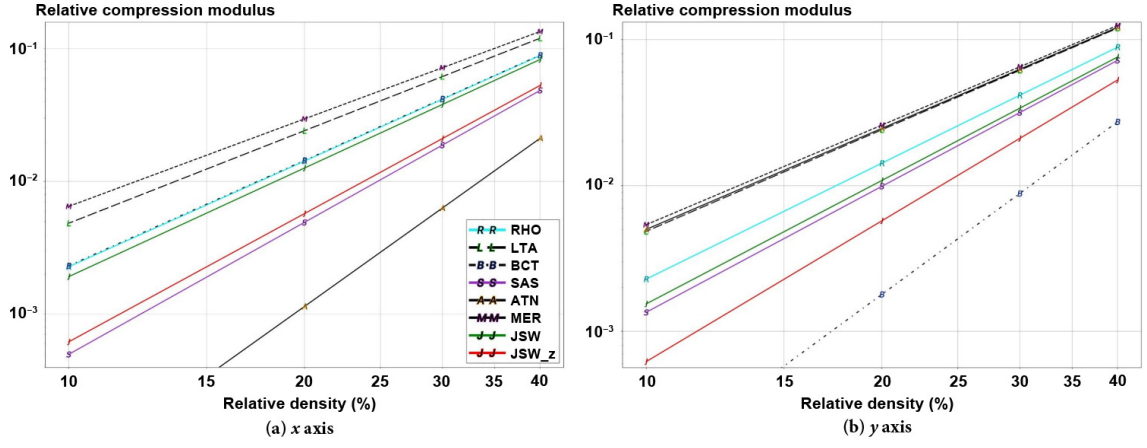

Fig. 15 Results of analysis of mechanical properties of single RVE from Fig. 14 using the Gibson–Ashby relation (Eq. (17)) in the case of compression: (a) along the x-axis and (b) along the y-axis; the line with triangles down (red) is dependent on the JSW-based structure at compression along the z-axis.

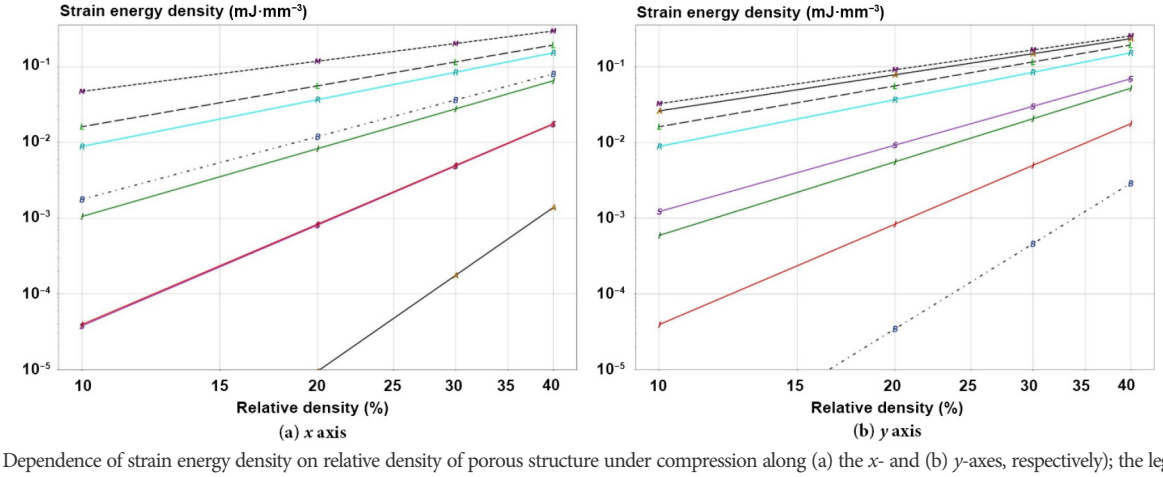

Fig. 16 Dependence of strain energy density on relative density of porous structure under compression along (a) the x- and (b) y-axes, respectively); the legend is the same as that in Fig. 15(a).

In total, Figs. 15 and 16 show that the effects of the topology and geometry are more evident at smaller relative densities of porous materials, and as the relative density increases, all the lines converge, and the effects of the topology and geometry become less explicit.

5 Conclusions

In this work, porous structures are generated on triply periodic surfaces (TPSs) via a previously developed method. The developed approach makes it possible to generate an unlimited number of new TPSs, on the basis of which new porous structures, composites, and metamaterials can be constructed. The thermal and mechanical properties of new porous structures are studied numerically via ANSYS and experimentally with samples manufactured via 3D printing from SBS filaments and polyamide PA-12. The results of the calculations are in good agreement with the experimental results. Thus, the results presented in the article indicate the effectiveness of our method for constructing TPSs and corresponding porous structures on the basis of atomic networks of natural crystals and provide the opportunity to select the most suitable structures for engineering applications from among those considered in the article in terms of their thermal and mechanical properties.

Acknowledgements

The research was supported by the Russian Science Foundation (Grant No. 22-23-00300).

Author contributions

Anton V. Eremin is responsible for Conceptualization (Equal), Data curation (Equal), Formal analysis (Equal), Funding acquisition (Lead), Investigation (Equal), Methodology (Equal), Project administration (Equal), Supervision (Equal), Writing - original draft (Equal), Writing - review & editing (Equal); Mikhail A. Frolov is responsible for Conceptualization (Equal), Data curation (Equal), Formal analysis (Equal), Investigation (Equal), Methodology (Equal), Validation (Equal), Writing - original draft (Equal), Writing - review & editing (Equal); Alexander F. Krutov is responsible for Conceptualization (Equal), Data curation (Equal), Formal analysis (Equal), Investigation (Equal), Methodology (Equal), Project administration (Equal), Supervision (Equal), Validation (Equal), Writing - original draft (Equal), Writing - review & editing (Equal); Mikhail I. Smolkov is responsible for Conceptualization (Equal), Data curation (Equal), Formal analysis (Equal), Investigation (Equal), Methodology (Equal), Resources (Equal), Software (Lead), Validation (Equal), Visualization (Equal), Writing - original draft (Equal), Writing - review & editing (Equal); Dmitry M. Bragin is responsible for Conceptualization (Equal), Data curation (Equal), Formal analysis (Equal), Investigation (Equal), Methodology (Equal), Validation (Equal), Visualization (Equal), Writing - original draft (Equal), Writing - review & editing (Equal); Andrey I. Popov is responsible for Conceptualization (Equal), Data curation (Equal), Formal analysis (Equal), Investigation (Equal), Methodology (Equal), Validation (Equal), Visualization (Equal), Writing - original draft (Equal), Writing - review & editing (Equal). All the authors have approved the final manuscript.

Availability of data and materials

The data that support the findings of this study is available from the corresponding author upon reasonable request.

Competing interests

The authors have no competing interests to declare that are relevant to the content of this article.

References

[1] Gibson LJ, Ashby MF. *Cellular Solids*. Cambridge (UK): Cambridge University Press, 1997.

[2] Silva T, Lu JY, Abu Al-Rub RK, *et al.* Investigation on tailoring the width and central frequency of bandgaps of TPMS structures. *Int J Mech Mater Des* 2024, **20**: 317–329.

[3] Wang ZY, Chen BZ, Lu YZ, *et al.* Mechanical properties and energy absorption of medium-entropy alloy triply periodic minimal surface cellular structures fabricated via selective laser melting. *Mech Mater* 2024, **196**: 105084.

[4] Günther F, Pilz S, Hirsch F, *et al.* Shape optimization of additively manufactured lattices based on triply periodic minimal surfaces. *Addit Manuf* 2023, **73**: 103659.

[5] Li ZT, Chen ZB, Chen XB, *et al.* Mechanical properties of triply periodic minimal surface (TPMS) scaffolds: Considering the influence of spatial angle and surface curvature. *Biomech Model Mechanobiol* 2023, **22**: 541–560.

[6] Yeranee K, Rao Y. A review of recent investigations on flow and heat transfer enhancement in cooling channels embedded with triply periodic minimal surfaces (TPMS). *Energies* 2022, **15**: 8994.

[7] Lin ZH, Pan JH, Li HY. Mechanical strength of triply periodic minimal surface lattices subjected to three-point bending. *Polymers* 2022, **14**: 2885.

[8] Maskery I, Aboulkhair NT, Aremu AO, *et al.* Compressive failure modes and energy absorption in additively manufactured double gyroid lattices. *Addit Manuf* 2017, **16**: 24–29.

[9] Baghous N, Barsoum I, Abu Al-Rub RK. Generalized yield surface for sheet-based triply periodic minimal surface lattices. *Int J Mech Sci* 2023, **252**: 108370.

[10] Wang YD, Lian YP, Wang ZD, *et al.* A novel triple periodic minimal surface-like plate lattice and its data-driven optimization method for superior mechanical properties. *Appl Math Mech* 2024, **45**: 217–238.

[11] Khedri E, Karimi HR, Aliha MRM, *et al.* Tensile, flexural, and mode-I cracking behavior of interpenetrating phase composites (IPC), developed using additively manufactured PLA-based structures with different infill densities and epoxy resin polymer as matrix. *Results Eng* 2024, **22**: 102162.

[12] Wallat L, Selzer M, Wasmuth U, *et al.* Energy absorption capability of graded and non-graded sheet-based gyroid structures fabricated by microcast processing. *J Mater Res Technol* 2022, **21**: 1798–1810.

[13] Xia Q, Zhu JX, Yu Q, *et al.* Triply periodic minimal surfaces based topology optimization for the hydrodynamic and convective heat transfer. *Commun Nonlinear Sci Numer Simul* 2024, **131**: 107819.

[14] Felix LC, Ambekar R, Tromer RM, *et al.* From pure mathematics to macroscale applications: The genesis of schwarzites. 2024: 2401.07884. https://arxiv.org/abs/2401.07884v1

[15] Pérez J. A new golden age of minimal surfaces. *Notices Amer Math Soc* 2017, **64**: 347–358.

[16] Cejka J, Morris RE, Nachtigall P. *Zeolites in Catalysis: Properties and Applications*. London (UK): The Royal Society of Chemistry, 2017.

[17] Fischer M. Adsorption of carbamazepine in all-silica zeolites studied with density functional theory calculations. *Chemphyschem* 2023, **24**: 202300022.

[18] Smolkov MI, Blatova OA, Krutov AF, *et al.* Generating triply periodic surfaces from crystal structures: The tiling approach and its application to zeolites. *Acta Crystallographica Section A* 2022, **78**: 327–336.

[19] Eremin AV, Frolov MA, Krutov AF, *et al.* Mechanical properties of porous materials based on new triply periodic and minimal surfaces. *Mech Adv Mater Struct* 2024, **31**: 11320–11336.

[20] Blatov VA, Shevchenko AP, Proserpio DM. Applied topological analysis of crystal structures with the program package ToposPro. *Cryst Growth Des* 2014, **14**: 3576–3586.

[21] Thompson MK, Thompson JM. *ANSYS Mechanical APDL for Finite Element Analysis*, Oxford (UK): Butterworth-Heinemann, 2017.

[22] Baerlocher C, McCusker LB, Olson DH. *Atlas of Zeolite Framework Types*. Amsterdam: Elsevier, 2007: 258–259.

[23] Arsentev MY, Sysoev EI, Makogon AI, *et al.* High-throughput screening of 3D-printed architected materials inspired by crystal lattices: Procedure, challenges, and mechanical properties. *ACS Omega* 2023, **8**: 24865–24874.

[24] Castañeda FD, García-Acosta G, Garzón-Alvarado DA, *et al.* Design for the additive manufacturing of structural elements with cellular materials using voronoi diagrams and delaunay triangulations: Biological and structural applications. *Mech Adv Mater Struct* 2024, **31**: 9550–9570.

[25] Xu YL, Pan H, Wang RN, *et al.* New families of triply periodic minimal surface-like shell lattices. *Addit Manuf* 2023, **77**: 103779.

[26] Shevchenko AP, Shabalin AA, Karpukhin IY, *et al.* Topological representations of crystal structures: Generation, analysis and implementation in the TopCryst system. *Sci Technol Adv Mater Meth* 2022, **2**: 250–265.

[27] NTop Documentation Release 4.0, available at https://support.ntop.com/hc/en-us/articles/360055403953-How-to-build-a-customlattice-unit-cell.

[28] Blatov VA. A method for topological analysis of rod packings. *Struct Chem* 2016, **27**: 1605–1611.

[29] Blatov VA, Delgado-Friedrichs O, O'Keeffe M, *et al.* Three-periodic

nets and tilings: Natural tilings for nets. *Acta Crystallogr Section A* 2007, **63**: 418–425.
[30] Fischer W, Koch E. New surface patches for minimal balance surfaces. *I. Branched catenoids. Acta Crystallographica Section A* 1989, **45**: 166–169.
[31] Porous 3D Documentation Release 1.0.1, available at https://p3d.topcryst.com/software/
[32] Cohen-Steiner D, Morvan JM. Restricted delaunay triangulations and normal cycle. In: Proceedings of the Nineteenth Conference on Computational Geometry–SCG'03. San Diego, California, USA. 2003: 312–321.
[33] Schoen AH. Reflections concerning triply-periodic minimal surfaces. *Interface Focus* 2012, **2**: 658–668.
[34] Brakke KA. The surface evolver. *Exp Math* 1992, **1**: 141–165.
[35] Shevchenko V, Balabanov S, Sychov M, *et al.* Prediction of cellular structure mechanical properties with the geometry of triply periodic minimal surfaces (TPMS). *ACS Omega* 2023, **8**: 26895–26905.
[36] Top N, Şahin İ, Gökçe H. The mechanical properties of functionally graded lattice structures derived using computer-aided design for additive manufacturing. *Appl Sci* 2023, **13**: 11667.
[37] Khaleghi S, Baghani M, Karimpour M, *et al.* Novel modified triply periodic minimal surfaces (MTPMS) developed using genetic algorithm. *J Mater Res Technol* 2023, **26**: 2881–2906.
[38] Formalev VF. *Thermal Conductivity of Anisotropic Bodies. Analytical Methods for Problem Solving.* Moscow (Russia): Fizmatlit, 2015.
[39] Kanit T, Forest S, Galliet I, *et al.* Determination of the size of the representative volume element for random composites: Statistical and numerical approach. *Int J Solids Struct* 2003, **40**: 3647–3679.
[40] Epov MI, Terekhov VI, Nizovtsev MI, *et al.* Effective thermal conductivity of dispersed materials with contrast inclusions. *High Temp* 2015, **53**: 45–50.
[41] Prajapati H, Ravoori D, Woods RL, *et al.* Measurement of anisotropic thermal conductivity and inter-layer thermal contact resistance in polymer fused deposition modeling (FDM). *Addit Manuf* 2018, **21**: 84–90.
[42] Elkholy A, Rouby M, Kempers R. Characterization of the anisotropic thermal conductivity of additively manufactured components by fused filament fabrication. *Prog Addit Manuf* 2019, **4**: 497–515.
[43] Scholz G, Gehringer M. *Thermoplastic Elastomers: At a Glance.* Boston (USA): De Gruyter, 2021.

Anton Vladimirovich Eremin. Doctor of Engineering Sciences. Head of Heat Power Department and Vice-Rector for Integration Projects, Samara State Technical University. Research interests: computational methods, thermodynamics.

Mikhail Alexandrovich Frolov. Candidate of Engineering Sciences, Assistant Professor of Department of General and Inorganic Chemistry, Engineer of Samara Center of Theoretical Materials Science, Samara Polytech, Samara, Russia. Research interests: chemistry, physics, and materials mechanics, continuum mechanics.

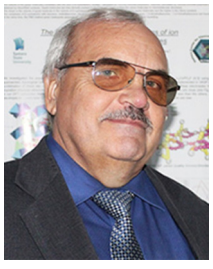

Alexander Fedorovich Krutov. Doctor of Physical and Mathematical Sciences, professor, Head of Laboratory of Computational Geometry and Theoretical Materials Science, PSUTI, Senior Research Officer of Samara Center of Theoretical Materials Science, Samara Polytech, Samara, Russia. Research interests: mathematical physics, relativistic theory of composite systems, theory of functional electron density, theoretical materials science.

Mikhail Igorevich Smolkov. Candidate of Physical and Mathematical Sciences degree seeking applicant, Research assistant of Laboratory of Computational Geometry and Theoretical Materials Science, PSUTI, Research Officer of Samara Center of Theoretical Materials Science, Samara Polytech, Samara, Russia. Research interests: computational geometry, computational mathematics, programming, machine learning.